High-Speed Path Length Scanning for Optical Coherence Tomography

by

Pei-Lin Hsiung

B.S.E., Electrical Engineering
Princeton University, 1997

Submitted to the

DEPARTMENT OF ELECTRICAL ENGINEERING AND COMPUTER SCIENCE

in partial fulfillment of the requirements for the degree of

MASTER OF SCIENCE

at the

MASSACHUSETTS INSTITUTE OF TECHNOLOGY

September 2000

Signature of Author_____
Department of Electrical Engineering and Computer Science
September 2000

Certified by_____
Professor James G. Fujimoto
Thesis Supervisor

Accepted by_____
Chairman, Department Committee on Graduate Students

High-Speed Path Length Scanning for Optical Coherence Tomography

by

Pei-Lin Hsiung

Submitted to the Department of Electrical Engineering and Computer Science
on September 5, 2000 in partial fulfillment of the requirements
for the degree of Master of Science

Abstract

Current optical coherence tomography (OCT) imaging technology allows acquisition of micron-scale images of tissue microstructure at rates of several frames per second over cross-sectional areas of a few square millimeters. These rates and ranges are limited by the mechanical scanning mechanism of the galvonometers currently employed in optical delay lines. New developments in OCT technology require a simple, high-speed scanning delay line capable of supporting broad spectral bandwidths. A portable, broadband, high-speed scanning technique would remove motion artifacts and allow ultrahigh resolution, spectroscopically-resolved OCT imaging to be performed *in vivo*, enabling OCT to be evaluated for detecting early neoplastic changes and cancers in a clinical setting.

This project develops and evaluates a novel high-speed delay line capable of scanning over several millimeters at a 1 kHz repetition frequency. The delay line uses a multi-pass mirror geometry based on a Herriott-type cell which accumulates differential delays in each pass. The delay line is electromagnetically-actuated using a commercially available audio speaker. The system enables image acquisition at a rate of 4 frames per second, allowing motion-artifact free *in vivo* images to be obtained.

The delay line was incorporated into the reference arm of an existing OCT system and evaluated during imaging of an anesthesized *Xenopus laevis* (African frog) tadpole, a common developmental biology model. Path length scanning over 3.1 mm at a 1 kHz repetition frequency is demonstrated. Higher scan repetition frequencies are feasible and are currently being investigated.

Thesis supervisor: Professor James G. Fujimoto
Department of Electrical Engineering and Computer Science

Acknowledgements

The research presented in this thesis would not have been possible without the resources of the ultrafast optics group at MIT. I wish to thank my research advisor, Professor Jim Fujimoto, for providing me the opportunity, the guidance, and the environment for completing the work presented in this thesis.

Xingde Li has been a mentor and supported this work with his all-around expertise, helpful suggestions and advice. Ingmar Hartl and Christian Chudoba have helped me debug countless systems as well as given me their friendship. I wish to thank Costas Pitris for technical assistance with the Macintosh system and for helpful discussions. The code-warriors Tony Ko and Ravi Ghanta have graciously modified the OCT data acquisition system repeatedly to help me test my delay lines. Drew Kowalevicz has been a good resource for ideas and for interesting discussions. Much gratitude also goes to Kathleen Saunders and Edny for their patience in sharing the *in vitro* OCT system. None of this work would have been possible without the help and advice of Fred Cote of the Edgerton Center Student Shop, who has given me his time and been patient with my odd tool requests and the magnetic iron filings which now reside permanently in the student shop.

Additional thanks go to John Fini, Juliet Gopinath, and Rohit Prasankumar, who have been wonderful officemates. They have provided advice, personality, textbooks, distractions, office supplies, and coffee...all very essential items in the daily grind of life as a graduate student.

My good friend and roommate Eden Miller has shared her humor, her insights, and her life with me for the past two years. I wouldn't have made it nearly this far without her friendship and support. Selen Altunata has also been a great friend and the crazy girl of our apartment, and both have been patient with me and my disappearances while finishing this thesis. My gratitude also goes to Rachel Prentice and STS, for humoring a would-be scientist despite the pedestal, and for providing a much needed life and culture break from the all-consuming environment of MIT.

Finally, I thank my family for their unconditional love, their support, and their understanding that I will, eventually, find my way on my own.

Contents

Chapter 1

Introduction

1.1 Motivation

Over the past two decades, medical imaging technology has advanced to give physicians the means to access indispensable information about the microscopic tissue anatomy of their patients. Imaging techniques such as computed tomography, magnetic resonance imaging, and high-frequency ultrasound have allowed physicians to non-invasively image structures in the human body with resolutions ranging from several millimeters to a hundred microns. For many diseases however, higher resolutions are necessary for earlier diagnosis to reduce patient morbidity. Techniques for detecting these diseases often suffer from sampling errors and processing artifacts associated with excisional biopsy, the current standard method for disease diagnosis.

To address these and other clinical issues, an imaging modality capable of resolving tissue architectural morphology and cellular features must be developed. Such a system should be non-invasive and capable of acquiring high resolution images at rates of several frames per second to avoid motion artifacts associated with imaging *in vivo*. This project investigates a novel high-speed optical delay line design for optical coherence tomography (OCT), a non-invasive imaging technique that can obtain high resolution images of tissue microstructure. A portable, high-speed optical delay line capable of supporting broad spectral bandwidths would

allow OCT to be used in the clinical setting to provide high resolution, spectroscopically-resolved *in vivo* images of tissue microstructure.

1.2 Background

Optical coherence tomography is an emerging medical diagnostic imaging technology developed at MIT which enables micron-scale, cross-sectional imaging of tissue microstructure *in situ* and in real time[1]. OCT imaging is similar to ultrasound B mode imaging except that it is performed by measuring the intensity of backscattered light rather than the echo delay of acoustical waves. OCT can function as a type of "optical biopsy" to permit the imaging of tissue microstructure with resolutions approaching that of standard excisional biopsy and histopathology. However, unlike biopsy and histology, OCT images are acquired in real time and without the need for removal of a tissue specimen[2-4]. Since OCT is optically based, images can also be acquired without direct contact with the tissue. OCT can therefore be interfaced with a wide range of medical devices such as catheters, endoscopes, hand held probes, and microscopes and can be used in combination with many current diagnostic techniques. Such a clinically-viable high resolution imaging technology may be used to guide biopsy to reduce patient morbidity and mortality in a variety of disorders where repeated biopsies are required. High resolution also allows OCT to detect neoplastic changes associated with many types of early stage pathologies. OCT therefore has potential to be used as a screening modality to detect and possibly grade cancers and increase the effectiveness of medical intervention.

OCT is based on a technique known as low coherence interferometry, previously applied in optoelectronic and fiber optic devices as well as in biological systems to perform optical ranging with micrometer resolution[5-7]Unlike ultrasound, which is performed by measuring the echo delay time for an incident ultrasonic pulse to be reflected from internal structures in tissue, OCT performs imaging by measuring the echo delay of light reflected from internal tissue structures[8-11]. Since the velocity of light is extremely high, measurement of optical echoes must be performed interferometrically. Figure 1.1 shows a diagram of a typical OCT system. One arm of the interferometer is a modular probe that directs light onto the sample and collects the reflected signal. The second arm includes a translating reference mirror or scanning delay line.

Optical interference between the light from the sample arm and the reference arm occurs only when the optical distance traveled by the light in both paths match to within the coherence length of the light source[1, 12-13]. In order to be useful for surgical guidance or screening, the reference arm path must be scanned quickly to provide the clinician with real-time imaging.

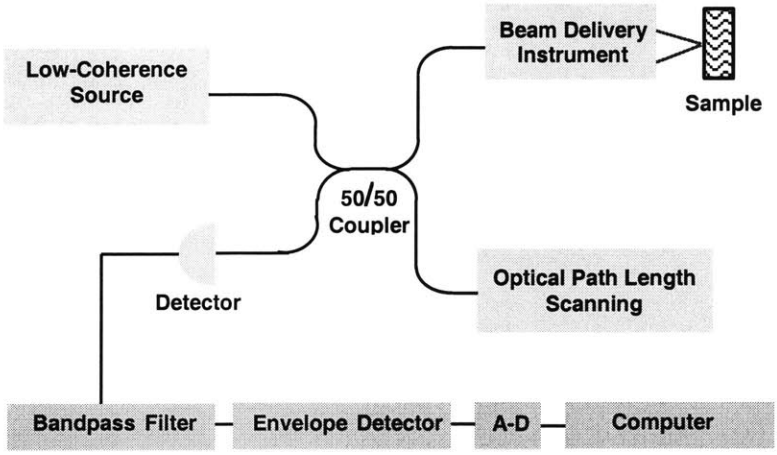

Figure 1.1 Schematic of an OCT interferometer imaging system implemented using fiber optics. OCT draws upon well-developed fiber optic communications technologies.

Current OCT imaging systems allow the acquisition of micron-scale images of tissue microstructure at rates of several frames per second over cross-sectional areas of a few square millimeters. These rates and ranges are limited by a number of factors. First, a high power laser source is required to provide adequate illumination over a short period of time. Second, a high-speed scanning delay line is required in the reference arm of the interferometer in order to produce interferometric data quickly. Last, the data acquisition and control electronics must allow image processing and display in real time. These factors are separate technological challenges that must be overcome to achieve OCT imaging at or near video rates.

Typical OCT systems employ a mechanically translating reference arm mirror to achieve axial scanning. Scan velocities for galvonometer-based scanning systems are limited by mechanical inertia to at most 60 cm/s with repetition rates of up to ~200 Hz. In order to remove motion artifact for imaging *in vivo*, image acquisition rates of several frames per second are necessary. To acquire a typical 3 mm depth image at 4 frames per second with 500 axial scans

per frame, a repetition rate of 2000 Hz would be necessary. This is equivalent to repeatedly scanning a reference mirror at 6 m/s over 3 mm. Piezoelectric optical fiber stretchers have been demonstrated at 600 Hz, but this technique is not temperature stable and suffers from birefringence effects that require extra components to compensate[14]. Grating-based phase delay lines developed from ultrafast laser technology have been shown to achieve 3 mm length scans at 1200 Hz and may be capable of achieving even higher scan rates[15, 16]. However, grating-based scanners have inherent bandwidth limitations which have not yet been fully investigated.

Advances in solid-state laser technology have allowed the development of ultrahigh resolution OCT imaging at 1-3 μm resolution[17, 18]. Broadband light sources used for ultrahigh resolution imaging can also be combined with spectroscopy to potentially enable functional OCT imaging[19]. Bringing these advances into the clinic requires a low cost, high-speed scanning system capable of supporting broad spectral bandwidths.

1.3 Statement of Work

This project develops and evaluates a novel, low-cost, high-speed delay line design based on an electromagnetically-actuated multi-pass cavity. The system uses a multi-pass mirror geometry based on a Herriott-type cell. Actuating one mirror in the cavity allows differential delays to accumulate in each pass. The delay line was incorporated into the reference arm of an existing OCT system and evaluated during imaging of an *in vivo* tissue sample. Path length scanning of over 3.1 mm at a 1 kHz repetition frequency is demonstrated for OCT imaging. Higher scan repetition frequencies are feasible and are currently being investigated.

Chapter 2

Path Length Scanning for Optical Coherence Tomography

2.1 Introduction

Optical coherence tomography performs optical ranging in tissue using a fiber-optic Michelson interferometer with a low-coherence illumination source. Since interference is observed only when the optical path lengths in the sample and in the reference arm paths match to within the coherence length of the source, precision distance measurements are possible if the source has a short coherence length. The amplitude of the reflected signal as a function of depth can be obtained by moving the reference arm of the interferometer at a constant velocity and filtering the interference fringes measured at the detector with a bandpass filter set at the heterodyne modulation frequency of the fringes. This frequency is often referred to as the Doppler frequency since it results from relative motion between the reference mirror and the sample in the sample arm. The filtered signal can be demodulated and digitized to produce a measurement of the optical backscatter or reflectance versus axial range. A cross-sectional image can then be constructed from a series of sequential axial scans recorded by translating the beam position across the sample. Alternatively, spectroscopic information can be acquired by digitizing and appropriately processing the full interference signal. This is illustrated in Figure 2.1.

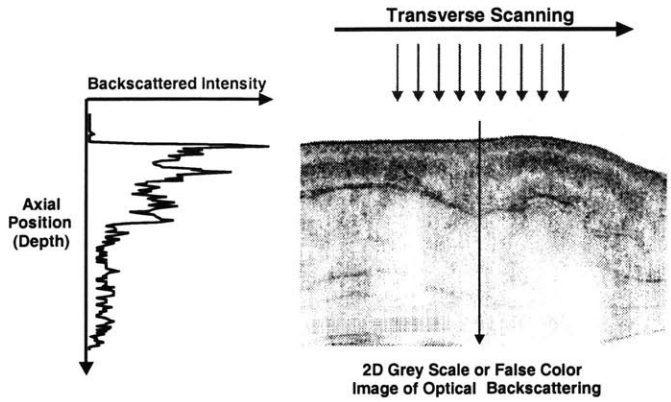

Figure 2.1 OCT generates cross-sectional images of tissue internal microstructure by scanning across the tissue to construct a two dimensional array of backscattered intensity in a cross sectional plane. A gray scale or false color image can then be displayed.

Since OCT relies on interferometry, information on the optical properties of tissue are obtained from one position in the sample at a time, with an axial resolution limited by the coherence length of the light source. High-speed scanning techniques must therefore be used to enable reference arm scanning at high enough rates to insure adequate sampling and to minimize image acquisition time. This chapter surveys techniques currently used to scan the optical group delay in the reference arm of an OCT system. The performance, advantages and disadvantages of each technique are presented.

2.2 Review of OCT Scanning Techniques

Developing rapid scanning optical delay lines has become an increasingly important area of research because of the increased significance of optical ranging techniques such as optical coherence domain reflectometry and optical coherence tomography[1, 5, 7]. These interferometric techniques require methods to scan the reference beam group delay at high speeds and linearity in order to enable high image acquisition rates. Techniques using spinning glass cubes and spinning mirror pairs have been demonstrated that have enabled extremely high scan velocities at high[20-22]. However, these techniques have nonlinear scan rates and can introduce delay-dependent dispersion which is unacceptable for ultrahigh resolution imaging with broad

bandwidth laser sources. This section discusses techniques currently used to achieve high-speed scanning for optical coherence tomography.

2.2.1 Linear Mechanical Scanning

Standard OCT systems use a mechanically scanning reference arm mirror to perform axial scanning. These mechanical scanners typically employ a galvonometer to rotate a small retroreflecting mirror mounted to a lever arm over the distance required for an axial scan (Figure 2.2). The retroreflector allows small angles of rotation to be converted to a linear displacement. The galvonometers used for these linear-scanning systems typically consist of a moving magnet rotor mounted between two stator coils, similar in structure to a torque rotor[23]. The stator coil produces a variable magnetic field, causing the rotor to turn in a controlled manner. Unloaded state-of-the-art galvonometers are capable of angular scanning over a few degrees with high linearity at frequencies approaching 1.5 kHz. A linear axial scan is possible because the galvonometer is heavily damped to prevent natural resonances.

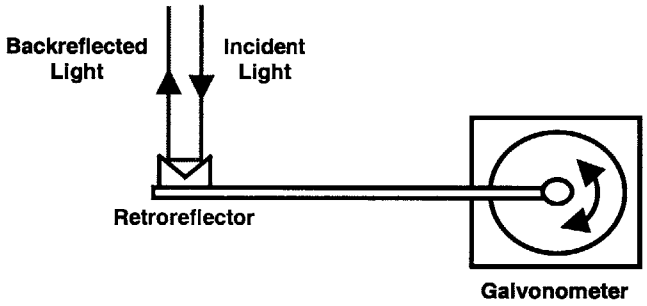

Figure 2.2 Delay line for linear mechanical scanning. Galvonometers used in this configuration are capable of scanning at repetition rates of up to ~200 Hz.

Scan velocities for linear galvonometer-based scanning systems are limited by the large forces necessary to drive a retroreflector mounted to a lever arm over the distance and at the speed necessary for an axial scan. For example, to acquire a typical 3 mm depth image at 4 frames per second with 500 axial scans per frame, a repetition rate of 2000 Hz would be necessary. This is equivalent to repeatedly scanning a reference mirror at 6 m/s over 3 mm. Scan velocities for galvonometer based scanning systems are limited by mechanical inertia to

approximately 60 cm/s with repetition rates of ~200 Hz, corresponding to roughly 200 axial scans per second. The mass of the mirror and lever arm must be minimized to achieve this performance. Despite the speed limitations of linear scanning, this technique has found widespread use in *in vitro* OCT systems and in *in vivo* ophthalmic applications because of its simplicity where rapid scanning is not critical. The lower heterodyne modulation frequency due to lower speed scanning also simplifies detection electronics. Bench-top *in vitro* systems utilizing linear mechanical scanners routinely operate with signal-to-noise ratios in excess of 110 dB.

2.2.2 Piezoelectric Optical Fiber Stretcher

In order to remove motion artifact for imaging of scattering tissue *in vivo*, image acquisition rates of several frames per second are necessary. Since this is not possible with linear mechanical scanning, high-speed imaging using piezoelectric optical fiber stretchers were investigated[14, 24]. One design for this delay mechanism consists of a long length of single mode fiber wrapped around several piezoelectric transducers (PZTs) fixed to a cylindrical housing (Figure 2.3). The combined structure is known as a piezoelectric modulator, or PZM. As a voltage is applied to the transducers, the PZT's polycrystalline ceramic material expands, stretching the fiber and changing the optical path length of the light guided within the fiber.

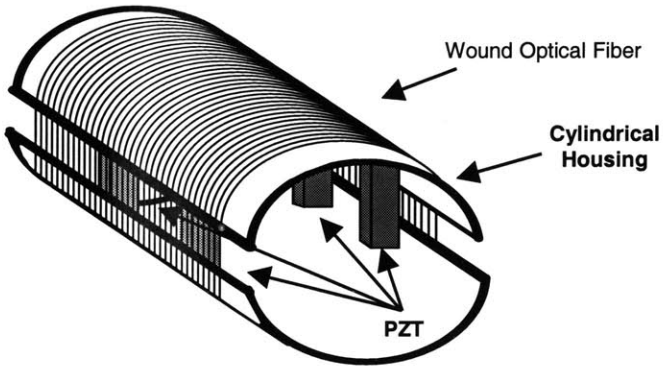

Figure 2.3 Schematic of fiber wound piezoelectric modulator used for rapidly scanning optical delay lines. As a voltage is applied to the transducers, the PZT's polycrystalline ceramic material expands, stretching the fiber and changing the optical path length of the light guided within the fiber

An alternate piezoelectric design has been patented which operates on a similar principle. The alternate design uses a planar geometry in which a long length of optical fiber is coiled upon one surface of a disc-shaped PZT[25, 26]. As the material expands, the change in the PZT diameter stretches the fiber and induces a change in the optical path length. The planar PZT design has the advantage of being more power efficient and simpler to cool than the cylindrical PZM design.

Both high-voltage and low-voltage PZTs are commercially available. Low-voltage PZTs are generally more commonly used because their electrical drive (100-200 Volts) units are easier to design and less costly. In order to provide more travel range, most low-voltage PZTs are packaged in stacks, allowing the expansion for a given voltage to be increased by the number of transducers in the stack. A major disadvantage of the low-voltage transducers is their high capacitance and intrinsic low heat conduction. PZTs are difficult to cool and overheating from the high-frequency voltage drives can destroy the transducer[27].

Piezoelectric optical fiber stretchers using low-voltage PZTs have been demonstrated to operate at 1200 axial scans per second, using 300 fiber windings and a 600 Hz modified triangular drive voltage waveform to minimize hysteresis[24]. Interferometric detection requires that the polarization states returned from the sample and reference arms of the interferometer be identical. It was found that static mismatch from wrapping the fiber around the PZM, thermal drift from frictional heating of the PZTs, and fast modulation from the voltage drive all contributed to polarization mismatch. A duplicate (unmodulated) sample arm structure with an identical number of fiber windings and a Faraday rotator in each arm were required to cancel the static and fast modulations. The reference arm PZM required temperature control to cancel the thermal drift.

The image acquisition rate of the piezoelectric scanning OCT system was sufficient to enable motion-artifact-free imaging of an *in vivo* embryonic *Xenopus laevis* (African frog), taken with a Kerr-lens mode-locked Cr:fosterite laser source[24]. The 300×250 pixel images could be obtained at a rate of 4 frames per second, using 2 mW of incident optical power in the sample

arm. The measured SNR ratio of the OCT system was 112 dB. A similar path length scanning system has also been used for *in vivo* OCT imaging of human oral mucosa[14].

Although PZT-based optical fiber stretchers have demonstrated performance at high-speeds, they suffer from a number of significant drawbacks. PZTs introduce hysteresis that cannot be fully compensated for by modifying the drive waveform. Hysteresis leads to dropout artifacts due to shifting of the heterodyne modulation frequency out of the detection bandwidth. Breakdown of the piezoelectric material due to heat generation poses an additional obstacle to scanning using the higher power required for high-speed. High power electronics are also difficult to integrate into clinical environments because of cost and safety concerns. Compensating for birefringence mismatch between the sample and the reference arms also requires extra components. Lastly, polarization mode dispersion becomes an issue due to the long fiber length required to produce the necessary optical path length delay. The necessary tolerances for the wavelength-dependent Faraday rotators and the need for matching of the PZMs in the two arms makes the technique unfeasible for future *in vivo* ultrahigh resolution and spectroscopically-resolved OCT systems which require support for large spectral bandwidths.

2.2.3 Phase Control Delay Line

An alternate technique that has been investigated is the use of a diffraction grating system to control the phase of the light in the reference arm to produce an optical group delay. The phase control concept is powerful because it allows a group delay to be produced by scanning the angle of an incident beam rather than by linear mechanical translation. Commercially available rotating beam scanners are typically one to two orders of magnitude faster than linear mechanical scanners. Optical beam scanning can also be performed by devices containing no moving components.

A grating-based phase control delay line produces an optical group delay by dispersing the optical spectrum of a beam and then applying a linear temporally modulated wavelength dependent phase. This is similar to grating-based techniques used for temporal shaping of ultrafast laser pulses and for chirped-pulse amplification[28, 29]. In typical realizations, the linear

wavelength dependent phase is applied by reflecting the optical spectrum of a beam from a tilted plane mirror (see Figure 2.4). If the angle of the mirror is rapidly scanned, a time dependent optical group delay is produced. The phase and group velocities can be independently scanned, allowing the heterodyne detection frequency and bandwidth to be set to optimize dynamic range. Grating-based phase control delay lines have been demonstrated for OCT that have allowed imaging with up to 2000 axial scans per second with signal-to-noise ratios upwards of 110 dB[15, 16].

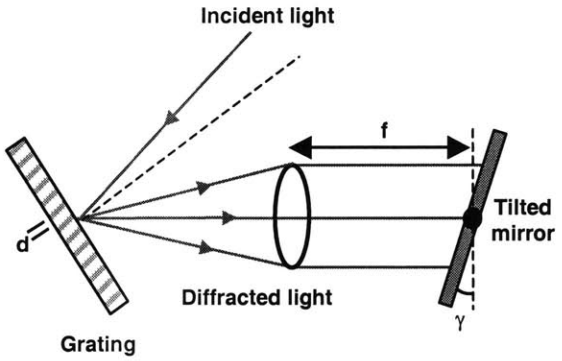

Figure 2.4 Schematic of grating-based phase delay line. Light is incident upon a grating with groove spacing *d*. The diffracted light traverses a lens that is separated from the tilted mirror by the focal length of the lens. Scanning the mirror angle γ produces a time-dependent optical group delay.

The scanning speed of a grating-based phase control delay line depends on the mechanism used to produce the angular beam scan. The fastest angular scanning for OCT to date has been achieved using a resonant galvonometer[16]. Resonant galvonometers are similar to galvonometers used for linear mechanical scanning except that they are designed to operate at or near their mechanical resonant frequency. Resonant scanners produce a sinusoidal change in angle as a function of time. Since the angle variation is sinusoidal, the usable linear range is limited to approximately 66% of the forward and backward scan and the detection bandwidth must be increased to accommodate the varying center frequency. The exact SNR loss depends on the noise-equivalent bandwidth of the particular system. However, since the resonant scanner can oscillate at speeds much higher than conventional beam scanners, this angular scanning method has potential for enabling real-time (24-30 frames per second) OCT imaging if the loss can be tolerated.

2.2.4 Alternative Angle Scanning Mechanisms

Alternative angular scanning mechanisms that have been proposed include polygonal scanning mirrors, holographic optical elements (HOEs), and acoustooptic modulators[30]. A polygonal scanning mirror consists of a machined polygon with highly reflecting facets. A repeatable angular scan can be produced by rotating the polygon with a high-speed motor and reflecting the beam off the facets. Since motors are available that can rotate up to 40,000 revolutions per minute, a polygonal scanning mirror with 24 facets could produce 16 kHz angular scans. Unlike galvonometer-scanned mirrors, however, polygonal scanning mirrors produce a combination of angular scanning and translation since the center of rotation is offset from the centers of the individual facets. This introduces a nonlinear component to the phase resulting in a nonlinear variation in both the phase and group velocities.

Holographic scanners also utilize rotating mirrors. A HOE consists of a rotating element that changes the transmitted diffraction angle of a beam as it is rotated. One configuration consists of a circular element with wedge subsections. Each wedge acts as a diffraction grating with a grating spacing that varies as a function of angle. As the element is rotated with a high-speed motor, the change in the grating spacing diffracts the beam at a different diffraction angle. The holographic scanner is usually used with monochromatic light since the grating will disperse a broad bandwidth source. The HOE could, in principle, replace both the grating for dispersing the spectrum and the angular scanner[30].

An acoustooptic modulator (AOM) is a device capable of beam scanning without using moving parts. A variable index of refraction grating can be produced using a small piezoelectric transducer to transfer sound energy to the crystal. When a radiofrequency signal is applied to the transducer, an acoustic wave is created in the crystal that varies the refractive index to produce a Bragg grating. As in the holographic scanner, light diffracted by the grating is transmitted through the crystal at an angle determined by the grating spacing. If the radiofrequency signal is varied, the grating spacing changes to produce a varying frequency shift in the light, scanning the angle of the incident beam.

2.3 Discussion

Since no cost-effective linear mechanical translator meeting the speed requirements necessary for *in vivo* imaging is available, alternative technologies have been investigated. To date, the phase control delay line has shown the best promise for realizing high-speed scanning in a clinical setting. The phase control delay line is robust, does not have high power requirements or suffer from the hysteresis of piezoelectric methods, and has better potential to realize video-rate *in vivo* imaging in a compact, portable system. However, the capability of the phase control delay line to support current broad bandwidth laser sources has not been well characterized. Alternative scan geometries based on a multi-pass cavity may be the best approach to enable high-speed scanning for ultrahigh resolution OCT systems.

Chapter 3

Herriott Cell Delay Line

3.1 Introduction

The ability to non-invasively obtain diagnostic information using "optical biopsy" could significantly impact the diagnosis and treatment of disease. An effective optical biopsy would obtain clinical information *in situ*, without removing tissue from the patient, thus eliminating scarring, pain, and the time and expense associated with excisional biopsy. Such an imaging modality would benefit patients with diseases in locations where it is hazardous to remove tissue (such as in the vascular and nervous system) and in diseases where multiple biopsies are required for diagnosis (such as adenocarcinoma for patients with Barrett's esophagus). Optical biopsies also allow the evolution of disease to be followed over time, enabling physicians to evaluate the effectiveness of pharmacological intervention.

An *in vivo* OCT imaging system capable of obtaining optical biopsies requires a path length scanning technique capable of high-speed. A high-speed delay line would enable imaging without artifacts associated with patient motion, allowing a physician to accurately assess tissue pathology. Advances in laser technologies have allowed the development of ultrahigh resolution OCT imaging at 1-3 μm resolution[17, 18]. Broadband light sources can also be combined with spectroscopy to enable functional OCT imaging[19]. Bringing these new advances into the clinic requires a low cost, high-speed scanning system capable of supporting broad spectral bandwidths.

This chapter discusses a novel, low cost, high-speed scanning delay line capable of scanning over several millimeters at a 1 kHz repetition frequency. The system enables image acquisition at a rate of 4 frames per second, allowing motion-artifact-free *in vivo* images to be obtained. The delay line uses a multi-pass mirror geometry based on a Herriott-type cell which accumulates differential delays in each pass. Multi-pass mirror delay scanners overcome the bandwidth limitations which are inherent in phase delay systems. The delay line is electromagnetically-actuated using a commercially available audio speaker. The low cost and low power requirement of the Herriott cell delay line makes it attractive for clinical and commercial use.

3.2 The Herriott Cell

Multi-pass optical cells were first reported in the mid-1960's by Herriott and co-workers[31, 32]. The use of confocal systems in optical maser oscillators led them to investigate the properties of interferometers formed using spherical mirrors at other than confocal spacings. They found that by using a beam misaligned with respect to the interferometer axis, a free-spectral range can be achieved which corresponds to an interferometer with a spacing that is several times greater than the actual spacing. The spot pattern observed on one of the mirrors ranged from traversing a line to tracing out an ellipse, and the number of spots was equal to the factor by which the apparent interferometer spacing exceeded the actual spacing.

Since the 1960's, Herriott cells have been employed in a variety of applications where long optical path lengths are an advantage. The cells are easy to construct and align, long paths can be achieved in a small volume, and interference fringes that arise in the cell can be effectively suppressed[33, 34]. Herriott cells have proven especially useful in laser spectroscopy, where the ability to fold a long path length into a small volume is useful for measuring species at low concentrations[35-37]. Advantages have also been found for Herriott configurations that use spherical mirrors that have been distorted so they are astigmatic and have a cylindrical component. The advantage of this modification is that the circulating optical beam more fully

fills the entire volume of the cell, using the mirror area more efficiently[32, 38]. Herriott has also investigated adding a small mirror within the cavity to perturb the beam onto a new elliptical path each time it strikes the perturbing mirror[32]. This also has the effect of increasing the maximum path length.

The electromagnetically-actuated optical delay line described in this chapter uses two broadband gold mirrors in a Herriott cell configuration which allows for near unity q-transform of the input beam through the cavity. A diagram of the cavity configuration is shown in Figure 3.1. One end of the cavity is scanned using a commercial audio speaker. The system can be operated in double-pass arrangement where the exit beam is reflected back into the cavity to allow direct coupling back into the reference arm.

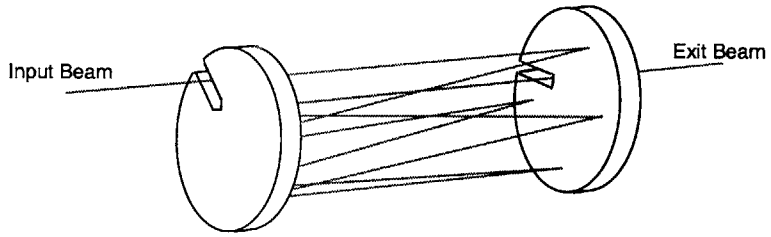

Figure 3.1 Schematic of multi-pass Herriott cell delay line. The cavity is formed using two symmetric broadband gold mirrors. Path length scanning is achieved by actuating one mirror of the cavity using an audio speaker.

The multi-pass cavity concept allows differential delays to be accumulated in each pass. The minimum required mirror displacement to achieve several millimeters of path length scanning can thus be reduced by increasing the number of bounces on the cavity mirrors. The multi-pass configuration allows scaling of controlled displacements of the end mirror by twice the number of bounces on the mirror, enabling high scan velocities to be achieved.

The maximum delay achievable using this method is limited by the spacing of the mirrors and the number of spots of finite size that can be spaced around the mirror without overlapping spots. Mirror reflectance is not a limiting factor by over an order of magnitude with present technology. A Herriott cell can also be designed to operate with near unity q-transform, allowing the beam parameters to remain unchanged regardless of the number of beam bounces on the

cavity mirrors. The near unity q-transform property of the Herriott delay line is attractive because it potentially minimizes parasitic modulation on the power coupled back into the reference arm an OCT system when the delay line is actuated, minimizing random intensity fluctuations which may invade the detection bandwidth and degrade the dynamic range of the system.

3.2.1 Bounce Pattern

A Herriott cell consisting of two coaxial mirrors is equivalent within the paraxial approximation to a series of equally spaced thin lenses as shown in Figure 3.2. The lenses have focal length f_1 and f_2 and are spaced by a distance d. The position x_n and slope x_n' of a ray just to the right of the n-th lens is completely specified by the input conditions x_0 and x_0'. The analysis can easily be extended to two dimensions to describe the beam position and slope in the y-plane.

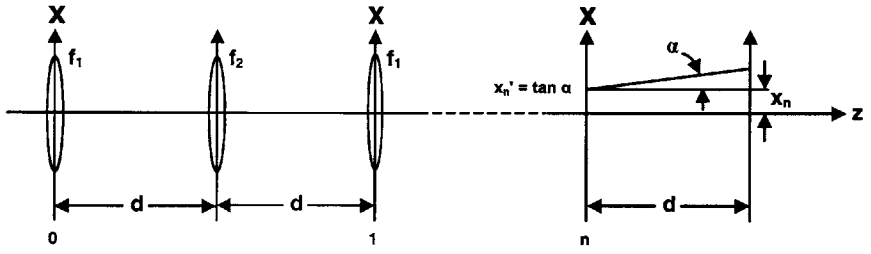

Figure 3.2 The unfolded Herriott cell is equivalent to a series of equally spaced thin lenses. The beam position (x_n, y_n) and slope (x_n', y_n') after the n-th round trip can be calculated from the initial beam position (x_0, y_0), the slope (x_0', y_0'), and the cavity parameters.

The equivalent Herriott cavity is shown in Figure 3.3. The lenses are represented by mirrors with radii of curvature $R_1 = 2f_1$ and $R_2 = 2f_2$.

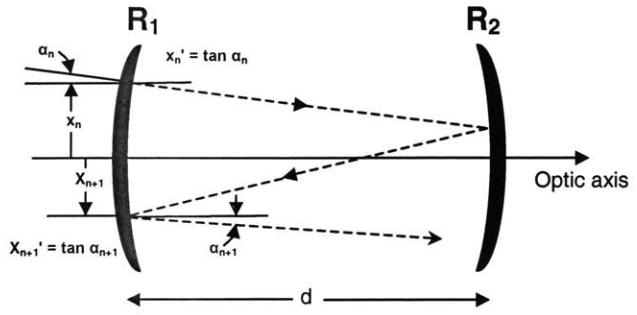

Figure 3.3 Schematic of a multi-pass resonator. Mirrors R_1 and R_2 refocus the beam on each bounce.

Using the resonator g-parameter convention[39], we can define the normalized parameters g_1 and g_2 by

$$g_1 = 1 - \frac{d}{R_1} \quad \text{and} \quad g_2 = 1 - \frac{d}{R_2}, \tag{3.1}$$

where d is the resonator length and $R_1 = 2f_1$ and $R_2 = 2f_2$ are the radii of curvature of the mirrors. It can be shown that the ray position x_n on mirror 1 after the n-th round trip can be written as

$$x_n = x_0 \cos n\theta + \frac{dg_2}{\sqrt{g_1 g_2 (1 - g_1 g_2)}} \left(x_0' - \frac{x_0}{R_1} \right) \sin n\theta, \tag{3.2}$$

where

$$\theta = \cos^{-1}(2g_1 g_2 - 1) \tag{3.3}$$

is the angle between successive reflected spots[39]. Corresponding expressions can also be written for y_n. These expressions hold for cavity separations such that $0 < g_1 g_2 < 1$, which corresponds to the regime where the resonator is stable. Equation (3.2) can be rewritten in the form

$$x_n = A \sin(n\theta + \alpha), \tag{3.4}$$

with

$$A^2 = {x_0}^2 + \frac{d^2 {g_2}^2}{g_1 g_2 (1 - g_1 g_2)} \left({x_0'}^2 - 2\frac{x_0 x_0'}{R_1} + \frac{{x_0}^2}{{R_1}^2} \right)^2 \tag{3.5}$$

and

$$\tan\alpha = \frac{x_0}{\frac{dg_2}{\sqrt{g_1 g_2(1-g_1 g_2)}}\left(x_0'^2 - 2\frac{x_0 x_0'}{R_1} + \frac{x_0^2}{R_1^2}\right)}. \tag{3.6}$$

The parameter A is the maximum possible excursion of the ray in the x direction for a given initial ray position x_0 and slope x_0'. A similar set of expressions can be obtained for the y coordinate:

$$y_n = B\sin(n\theta + \phi) \tag{3.7}$$

$$B^2 = y_0^2 + \frac{d^2 g_2^2}{g_1 g_2(1-g_1 g_2)}\left(y_0'^2 - 2\frac{y_0 y_0'}{R_1} + \frac{y_0^2}{R_1^2}\right)^2$$

$$\tan\phi = \frac{y_0}{\frac{dg_2}{\sqrt{g_1 g_2(1-g_1 g_2)}}\left(y_0'^2 - 2\frac{y_0 y_0'}{R_1} + \frac{y_0^2}{R_1^2}\right)}.$$

Equations (3.4)-(3.7) show that the collection of points where the ray intersects the mirror in general traces out an ellipse. In the special case where $A = B$, the points trace out a circle. This is illustrated in Figures 3.4:

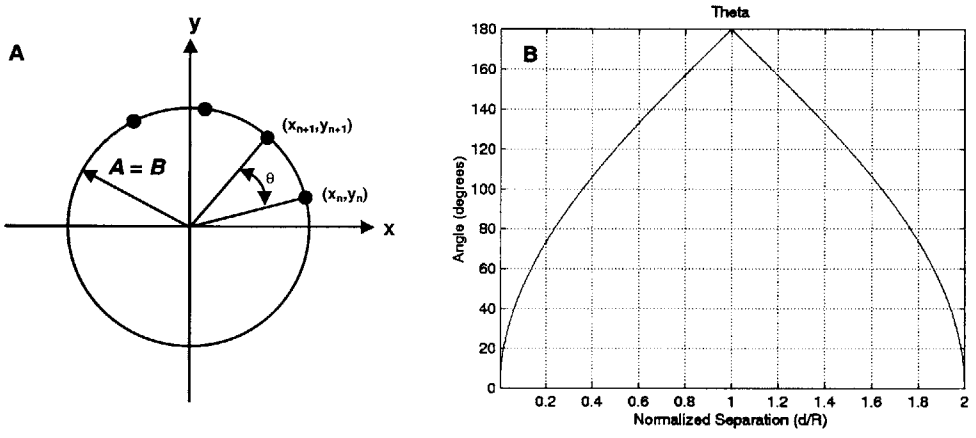

Figure 3.4 A. Projection of the beam intersection points on the mirror for the case $A = B$. B. The angle θ as a function of the normalized cavity separation.

The ray walks in a sinusoidal pattern along the surface of the mirrors, with a characteristic frequency determined entirely by the radius of curvature of the mirrors and the cavity separation[35]. The eccentricity of the ellipse is determined by a combination of the cavity configuration and the input conditions (eqns. (3.5) and (3.7)).

Herriott pointed out an important special case when the resonator dimensions are such that $n\theta = 2\pi K$, when n and K are integers. After n round trips, the beam returns exactly to the entrance point, allowing the beam to retrace the same path indefinitely. The ratio between the focal lengths and the cavity separation completely determine whether a closed path is traced [31]. More complicated ray paths are possible if astigmatic mirrors are used. In this case the oscillation frequencies θ are different in the x and y directions, leading to Lissajous patterns that can more fully fill the volume of the Herriott cell[32].

3.2.2 Stability

Variations in the mirror radii of curvature, cavity length, and mirror tilt angle will cause the beam spots to move from their ideal positions. This presents a problem for the Herriott cell delay line if the spot drift causes the exit beam to clip on the mirror slot or even wander off the mirror surface as the mirrors are actuated. The motion of the spots when the cavity length is varied during actuation must also be minimized to minimize parasitic modulation of the reference arm power. This section will discuss methods to model the beam parameters when the cavity length of the delay line is varied. Tolerance on errors in the mirror radii of curvature, cavity length, and mirror tilt will also be established.

Beam Parameters

In order to understand how the multi-pass cavity affects the parameters of the beam in the reference arm, the cavity was first modeled based on the ABCD matrix formalism using a standard mathematical modeling package. The beam trajectory through the cavity can be analyzed to determine alignment stability to small mirror displacements. The beam bounce

pattern for different mirror focal lengths, cavity separations, input beam angles, and input beam parameters can be varied independently to determine the orientation and beam parameters of the output beam.

ABCD matrices can be used to design the imaging characteristics of multi-pass imaging systems. The Herriott cell can be completely modeled using two matrices:

$$D(d) := \begin{bmatrix} 1 & d \\ 0 & 1 \end{bmatrix}, \tag{3.8}$$

describing propagation through a free space distance d, and

$$F(f) := \begin{bmatrix} 1 & 0 \\ \frac{-1}{f} & 1 \end{bmatrix}, \tag{3.9}$$

describing the action of a lens of focal length f. Multiplying the matrices together results in an equivalent ABCD matrix describing the action of the cascaded optical system, i.e.

$$M_{sp} = \begin{bmatrix} A & B \\ C & D \end{bmatrix} = \left(D(d)F(f)\right)^2 = \begin{bmatrix} \left(1-\frac{d}{f}\right)^2 - \frac{d}{f} & 2d - \frac{d^2}{f} \\ \frac{d}{f^2} - \frac{2}{f} & 1 - \frac{d}{f} \end{bmatrix}, \tag{3.10}$$

which describes one pass through a symmetric Herriott cavity.

This matrix can be cascaded n times to produce an equivalent ABCD matrix M_{eq} to describe an n-bounce Herriott cavity. The equivalent matrix terms for a cavity with 21 bounces on each mirror is shown in Figures 3.5a and 3.5b.

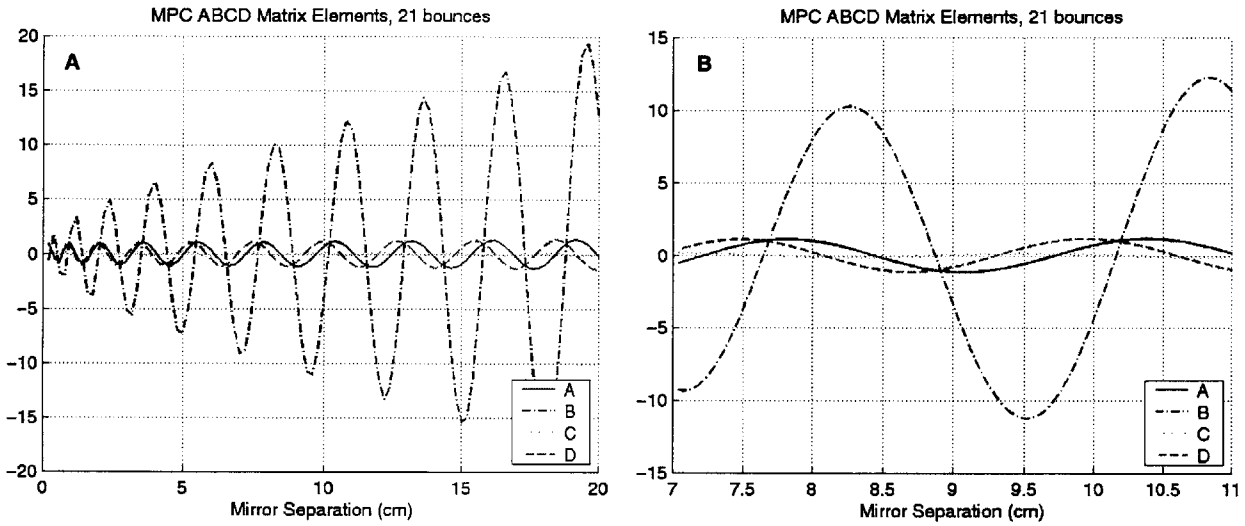

Figure 3.5 A. ABCD matrix terms for a cavity using mirrors with a 10.16 cm focal length and 21 bounces on each mirror. B. Terms near the 9.2 cm operating point for the configuration demonstrated in this chapter.

It can be seen from Figure 3.5 that the values for the matrix terms oscillate with increasing amplitude and decreasing frequency as the cavity separation is increased. For values of cavity separation where A = ±1, B = 0, C = ±1, and D = 0, the M_{eq} acts as a unity matrix and the cavity has no effect on the beam confocal parameter.

The effect of the cavity on the beam as the end mirror is actuated may also be analyzed by modeling the slope of the same ABCD matrix terms as a function of cavity separation. Figures 3.6a and 3.6b show the slope of the ABCD matrix terms for the cavity described in Figure 3.5.

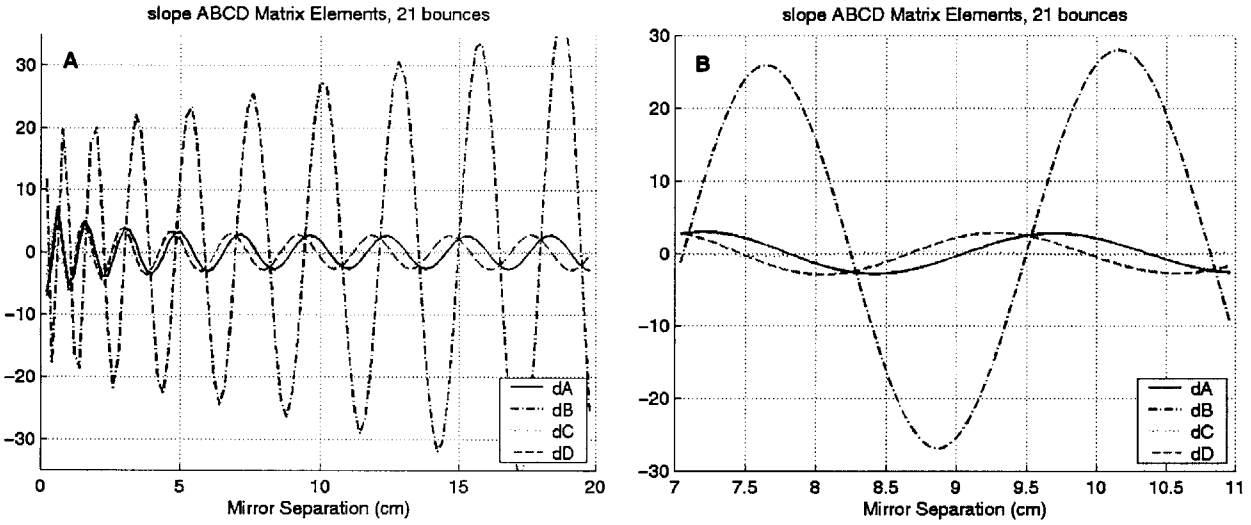

Figure 3.6 A. Slope of the ABCD matrix terms for the cavity in Figure 3.5. B. Slope terms near the 9.2 cm operating point for the configuration demonstrated in this chapter.

The equivalent matrix M_{eq} can also be used to describe the beam in two orthogonal planes. The equivalent matrix in each plane determines the exit beam parameters in that plane. The spot pattern on the mirrors can also be analyzed by plotting the position of the beam at the end mirrors using the ABCD matrices. Minimizing the slopes of the matrix terms theoretically minimizes the change in the beam parameters as the cavity end mirror is actuated. In order to minimize parasitic modulation of the power in the reference arm, the mirror separation should be adjusted to minimize the change in the matrix terms when the cavity length is varied.

It can be seen from Figure 3.6s that it is difficult to determine an optimum operating point that minimizes the slope of all the matrix terms. Figures 3.5b and 3.6b illustrate that the experimentally determined operating point does not in fact correspond to either a unity transform configuration for the cavity or a point of minimum matrix term slope. It is important to note that the ABCD matrix and q-parameter methods are paraxial formalisms which assumes that all beam angles are small relative to direction of propagation. Since this approximation cannot strictly be made due to the large bounce angles of the reference arm beam inside the cavity, the ABCD matrix model was used only as a guideline to experimentally determine the optimum alignment to couple as much of the reference beam as possible back into the reference arm while

minimizing parasitic modulation. The affects of astigmatism and chromatic aberration within the cavity have also been ignored in this model.

Mirror Radii and Cavity Length Tolerance

An alternate method to evaluate the error tolerances of the Herriott cavity is to consider the motion of the spots due to variations in the cavity separation, errors in the mirror radii, and errors in the mirror tilt. The tolerances are set by the condition that the exit beam must be separable and not overlap with any other beam. The ideal configuration would entirely eliminate the dependence of the exit beam position on the cavity length, allowing the cavity to be actuated without beam deviation. For simplicity, symmetric resonators with $g_1 = g_2 = g$ and circular spot patterns on the end mirrors will be discussed in this section.

For N transits between resonator mirrors, the angle between adjacent spot centers is given by[35]

$$\beta = \frac{4\pi}{N+1}. \tag{3.11}$$

The angle between successive bounces is given by the cavity parameters specified in equation (3.3). For equally spaced spots, θ is an integer J multiple of β, where J represents the number of times the spots walk around the mirror before exiting the cavity (Figure 3.7).

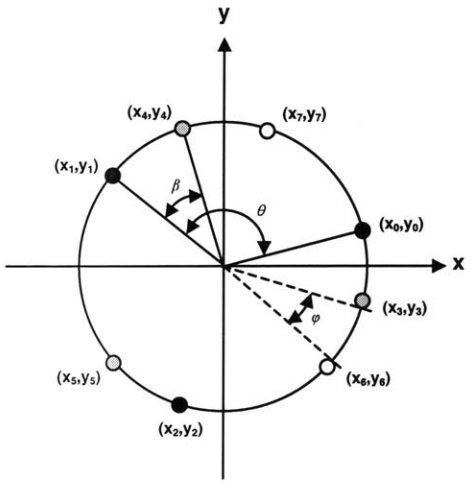

Figure 3.7 Diagram illustrating a bounce pattern on the mirror for the condition $J = 4$.

Assuming a spot diameter of $3\omega_m$ on the mirror, the angle φ between adjacent spot edges is

$$\varphi = \beta - [(3\omega_m)/r_m], \tag{3.12}$$

where $3\omega_m$ represents the Gaussian spot size and r_m represents the radius of the circle of spots on the mirrors. If there is an error in the mirror g parameter Δg, the error in θ is given by

$$\Delta\theta \approx \frac{d\theta}{dg} \times \Delta g = \frac{-2\Delta g}{\sqrt{1-g^2}}. \tag{3.13}$$

If no two spots overlap, the accumulated error for $(N\text{-}1)/2J$ round trips must not exceed φ[35]. Thus

$$|\Delta g| \leq \frac{J\sqrt{1-g^2}}{N-1}\left(\frac{4\pi}{N+1} - \frac{3\omega_m}{r_m}\right). \tag{3.14}$$

In terms of tolerances in the mirror radii ΔR and cavity length Δd,

$$\Delta g \cong \frac{-\Delta d}{R} + \left(\frac{d}{R^2}\right)\Delta R \tag{3.15}$$

For the 42 transit cell (21 spots per mirror) demonstrated in this chapter, the R = 20.32 cm radii mirrors are separated by d = 9.2 cm. The spots walk in a circle roughly 5 mm from the 2.54 cm mirror rims, traversing J = 7 circuits around the mirror before exiting the cell. Assuming a spot size of 2 mm and a maximum of 1 cm error in the mirror radii, the tolerance on the cavity length is a reasonable 3 mm. This scale corresponds well to the experimentally determined values of the cavity tolerance.

Mirror Tilt Tolerance

The optic axis for a resonator with two spherical mirrors is defined as the line connecting the center of curvature of the two mirrors. If one of the mirrors is tilted, the optic axis of the system also tilts. For a Herriott resonator, this has the effects of distorting the generally elliptical spot pattern and moving the center of the ellipse along the optic axis. Trutna and Byer proposed a geometric analysis that calculates the displacement of the mirror spots by assuming that the effect of the mirror tilt can be described by fixing the optic axis and attributing an error in position and slope to the input beam[35]. Transforming the result from the new optic axis coordinate system to the original system allows the deviation of the spots from their original positions to be calculated.

Suppose the multi-pass resonator consists of two spherically curved mirrors depicted in Figure 3.8. The centers of curvature of mirrors 1 and 2 are *C1* and *C2*, respectively.

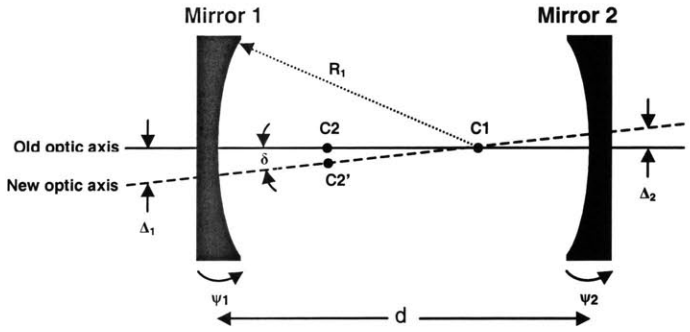

Figure 3.8 Diagram showing the effect of mirror misalignment on the resonator. Tilting mirror 2 causes the center of curvature of the mirror to move, defining a new optic axis.

If mirror 2 is tilted about its *y*-axis by an amount ψ_2, the center of mirror 2 moves to a new position *C2'*, defining a new optic axis. The angle δ between the old and the new axis is[35]

$$\delta = \frac{(1-g_1)\psi_2}{(1-g_1 g_2)}. \tag{3.16}$$

The displacement of the optic axis in the *x*-direction on mirror 1 is

$$\Delta_1 = \frac{d\psi_2}{(1-g_1 g_2)} \tag{3.17}$$

and the displacement of the optic axis in the x-direction on mirror 2 is

$$\Delta_2 = \frac{-g_2 d\psi_1}{(1-g_1 g_2)}. \tag{3.18}$$

The analysis can be repeated assuming that mirror 1 is rotated about an angle ψ_1. The resulting displacement angles and positions are

$$\delta = \frac{(1-g_2)\psi_1}{(1-g_1 g_2)}, \tag{3.19}$$

$$\Delta_1 = \frac{d\psi_1}{(1-g_1 g_2)},$$

$$\Delta_2 = \frac{-g_1 d\psi_1}{(1-g_1 g_2)}.$$

From the previous discussion of the Herriott cell, the position of the n-th bounce on mirror 1 was given to be

$$x_n = F_n(x_0, x_0') = x_0 \cos n\theta + \frac{dg_2}{[g_1 g_2 (1-g_1 g_2)]^{1/2}} \left(x_0' - \frac{x_0}{R_1} \right) \sin n\theta. \tag{3.20}$$

The error in beam displacement on mirror 1 on the n-th bounce can be determined from errors in the initial beam displacement Δx_0 and $\Delta x_0'$ slope. The error can be written as

$$\Delta x_0 \cong \frac{\partial F_n}{\partial x_0} \Delta x_0 + \frac{\partial F_n}{\partial x_0'} \Delta x_0' \tag{3.21}$$

or

$$\Delta x_n \equiv \Delta x_0 \cos n\theta + \frac{dg_2}{[g_1 g_2 (1 - g_1 g_2)]^{1/2}} \left(\Delta x_0' - \frac{\Delta x_0}{R_1} \right) \sin n\theta . \qquad (3.22)$$

For a rotation of mirror 2 about ψ_2, the error on mirror 1 becomes

$$\Delta x_n = \frac{d\psi_2}{(1 - g_1 g_2)} \cos n\theta , \qquad (3.23)$$

and for a rotation of mirror 1 about ψ_1, the error on mirror 1 becomes

$$\Delta x_n = \left(\frac{g_2}{g_1} \right)^{1/2} \frac{d\psi_1}{(1 - g_1 g_2)} \cos\left[n\theta + \cos^{-1} (g_1 g_2)^{1/2} \right] \qquad (3.24)$$

The last two expressions (3.23) and (3.24) give the distortion of the spot pattern in terms of the coordinate system of the new optic axis. Transformation to the original coordinate system is accomplished by subtracting the optic axis displacement[35]. Therefore, if mirror 1 is tilted by an angle ψ_1, the n-th spot on mirror 1 deviates from its original position by an amount

$$\Delta x_n = \left(\frac{g_2}{g_1} \right)^{1/2} \frac{d\psi_1}{(1 - g_1 g_2)} \left\{ \cos\left[n\theta + \cos^{-1} (g_1 g_2)^{1/2} \right] - (g_1 g_2)^{1/2} \right\}. \qquad (3.25)$$

For a rotation ψ_2 of mirror 2, the deviation of the n-th spot on mirror 1 is

$$\Delta x_n = \frac{d\psi_2}{(1 - g_1 g_2)} (\cos n\theta - 1). \qquad (3.26)$$

Since the input beam is externally controlled, the $n = 0$ spot does not move when the mirrors are tilted. This is verified in equations (3.25) and (3.26)[35].

Figure 3.9 shows a plot of the spot deviation for the first four spots on mirror 1 for R = 20.32 cm radii of curvature symmetric mirrors. The plot corresponds to ψ_1 = 1 milliradian of

mirror 1 tilt, allowing the deviation in mm/mrad to be plotted. A tilt of 5.6 mrad corresponds to the maximum possible tilt of the mirror when it is actuated to produce 3 mm of optical delay.

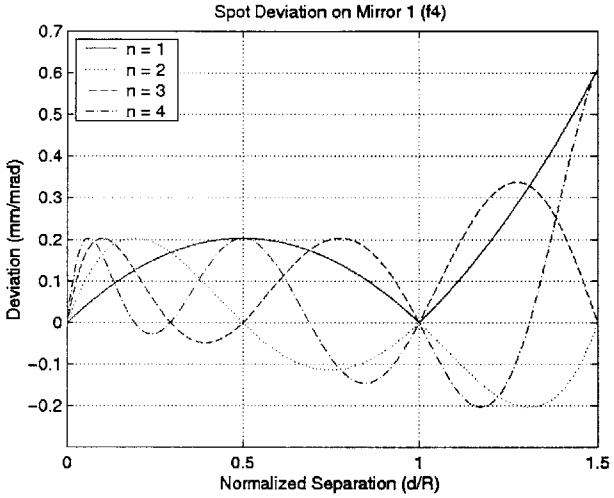

Figure 3.9 Plot of spot deviation versus normalized cavity separation for the first 4 round trips on mirror 1. The number of zero deviation configurations increases with the number of round trip passes.

The amount of deviation a spot experiences is seen to be a minimum for all spots at the confocal cavity configuration, $d/R = 1$. Spot deviation increases without bound as the cavity becomes unstable ($d/R = 2$). The numerical value of the deviation scales linearly with the mirror radii independently of the normalized cavity separation. The deviation curve also intercepts zero deviation points with increasing frequency as bounce number increases.

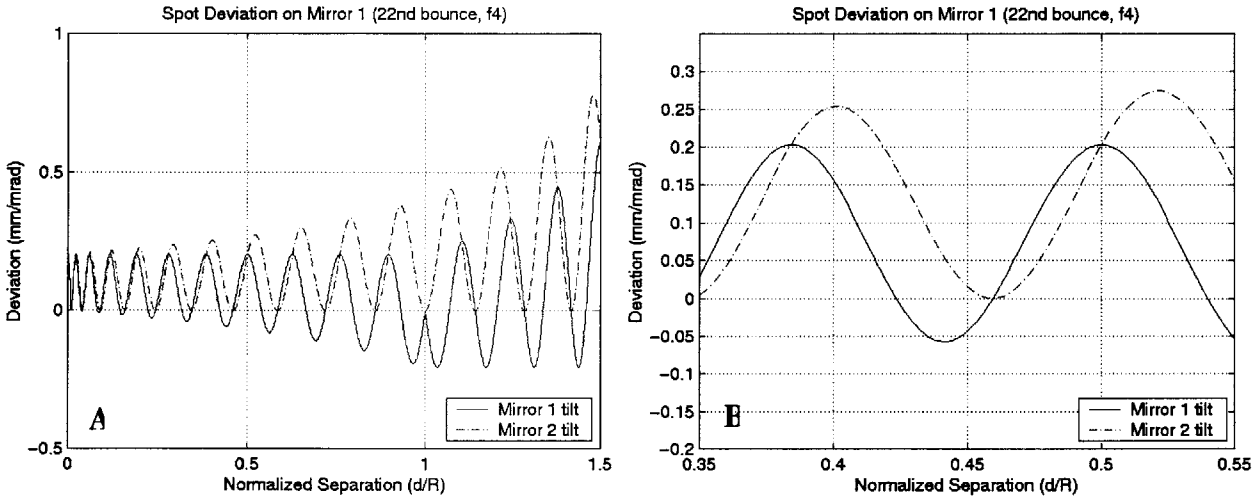

Figures 3.10 Plot of spot deviation versus normalized cavity separation for the 22nd round trip.

Figures 3.10 above plot the spot deviation on mirror 1 for the $n = 22$ spot corresponding to the exit beam used for the Herriott cell demonstrated in this chapter. As can be seen in Figure 3.10, a number of cavity configurations can be chosen to minimize motion of the exit beam if the mirror is tilted during actuation. The cavity separation of 9.2 cm corresponds closely to the zero deviation point of $d/R = 0.46$ for mirror 1 actuation shown in Figure 3.10.

The results of this section indicate that the first step in designing a multi-pass scanning delay line is to decide on the desired number of transits. For a specified number of transits there are several possible resonator designs. The cavity configuration chosen is set by the limitations on mirror size and input beam angle and position required to allow the desired number of spots to fit on the mirror without overlapping. The mirror radii of curvature chosen should be as small as possible within this limitation to minimize the beam deviation due to mirror tilt.

3.3 Actuation

For dynamic actuation, one end of the multi-pass cavity was driven with a commercially available audio speaker. Audio speakers are inexpensive, optimized for operation in the audio frequency range from 20 to 20,000 Hz, and have relatively modest power requirements. Audio speakers could therefore easily operate at a scanning frequency high enough to enable video-rate (26-30 frames per second) OCT imaging.

3.3.1 Harmonic Oscillator Model

An audio speaker consists of a coil of conducting wire surrounding a strong magnet and suspended by a rigid cone. The upper outer portion of the wire coil is attached to the center of the cone while the outside rim of the cone is attached to a rigid metal housing via a flexible brim (Figure 3.11). Not shown is an elastic membrane fixed above the magnet that attaches the copper coil to the metal housing. When an alternating electric current is driven through the wire coil, an alternating magnetic field is electromagnetically generated within the coil, causing the coil and

the attached cone to actuate. The moving cone generates an acoustic wave with a frequency equal to the frequency of the drive waveform.

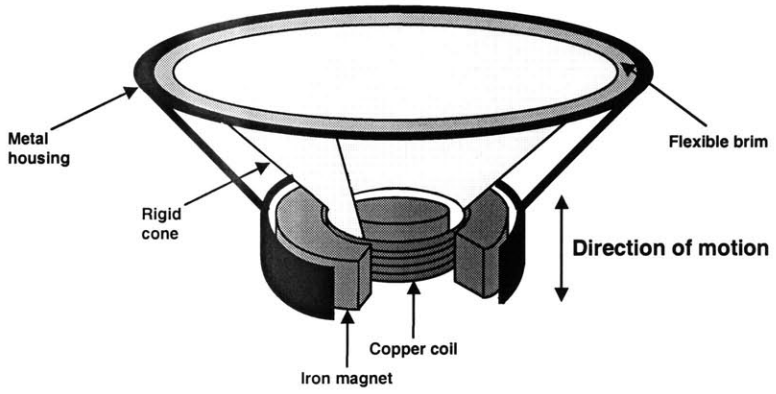

Figure 3.11 Cutaway view of a speaker coil and magnet. Passing an alternating current through the coil causes the coil to actuate at the frequency of the driving voltage.

Dynamic operation of the speaker system can be modeled using a damped simple harmonic oscillator model. The equation of motion for the model is given by

$$m\frac{d^2x(t)}{dt} + \gamma\frac{dx(t)}{dt} + kx(t) = f(t), \tag{3.27}$$

where m refers to the mass of the load (wire coil, mirror, membrane, and cone), γ is the damping coefficient due to air, and k is the coefficient of the restoring force provided by the membrane. The driving force of the system is represented by $f(t)$ and the displacement of the mirror is represented by $x(t)$. If the driving force and the displacement are expressed in the frequency domain, equation (3.27) becomes

$$-m\omega^2 X(\omega) + \gamma i\omega X(\omega) + kX(\omega) = F(\omega). \tag{3.28}$$

Letting $\omega_0^2 = k/m$, this can be rewritten in the form of a system transfer function:

$$\frac{X(\omega)}{F(\omega)} = \frac{1}{m} \frac{(\omega_0^2 - \omega^2) - i\gamma_m \omega}{(\omega_0^2 - \omega^2)^2 + \omega^2 (\gamma_m)^2}. \tag{3.29}$$

As the input drive frequency increases, the displacement decreases. In the case of relatively low damping, the displacement scales roughly linearly with the drive waveform. In the limiting case when the drive frequency $\omega \to \infty$, $1/\omega^2 \to 0$, and the mirror displacement shrinks quadractically toward zero. The mass term must be kept as small as possible to maximize the scan length for a given drive amplitude.

3.3.2 System Response and Transfer Function

The transfer function of equation (3.29) can be used to design an optimum drive waveform to maximize the usable linear scan of the delay line. The optimum scan characteristic is a position versus time function following a triangular waveform. A triangular waveform allows two scans to be acquired in one period of the waveform, thus enabling the generation of two axial scans in one drive cycle. Every other axial scan can be registered and spatially inverted during data acquisition. An approximation to the ideal drive waveform can be found by using a Fourier series expansion to determine the drive $f(t)$ in the time domain given a desired $x(t)$.

The desired triangular position versus time function $x(t)$ can be expanded in a Fourier series

$$x(t) = \sum_n b_n \sin(n\omega_0 t) = \sum_n \frac{A}{(n\omega_0)^2} \sin\left(n\omega_0 \tfrac{T}{4}\right) \sin(n\omega_0 t), \tag{3.30}$$

where ω_0 is the angular frequency of the drive and T is the drive period. The amplitude of the frequency components $X(\omega)$ are given by

$$X(\omega) = \frac{A}{\omega^2} \sin\left(n\frac{\pi}{2}\right). \tag{3.31}$$

From equation (3.31), we can find the ideal drive $f(t)$ for high frequencies by taking the inverse Fourier Transform of $\omega^2 X(\omega)$,

$$f(t) = IFT\left[A\sin\left(n\frac{\pi}{2}\right)\right] = \pm A\delta(t), \tag{3.32}$$

for $\sin(n\pi/2) = \pm 1, 0$ otherwise. The ideal drive waveform to produce a perfectly linear scan is a series of delta functions. Unipolar and bipolar square waves with programmable duty cycles can be tested to determine the best approximation to the optimum drive.

3.3.3 Results

The range and linearity of the speaker motion was characterized by mounting a small, flat mirror at the center of the speaker coil and incorporating the system into one arm of a Michelson interferometer. The number of interferometric fringes generated when the speaker is actuated can be analyzed to determine the position of the mirror as a function of time, drive voltage amplitude, and drive waveform. The velocity of the mirror as a function of scan position can also be extracted from the interferometric data to determine the linearity of the scan.

Range and Velocity

The motion of the mirror was characterized using a sinusoidal drive waveform. Different speakers were tested in both vertical and horizontal mount configurations with different mass mirrors. It was found that the motion of the coil and mirror was better aligned with the direction of travel when the speaker was oriented vertically. A vertical orientation was therefore used for all further measurements.

Figure 3.12 shows the displacement and velocity of the mirror versus peak-to-peak drive voltage for a 1.6 gram and a 0.8 gram plane mirror actuated with a 500 Hz sinusoidal drive waveform.

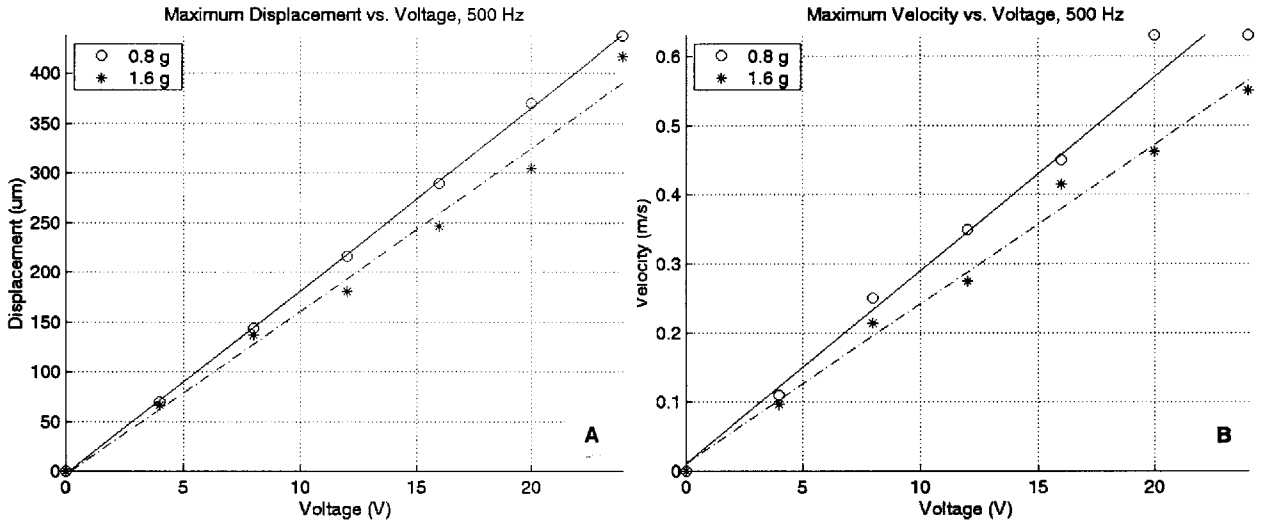

Figure 3.12 Displacement (A) and maximum velocity (B) versus voltage for a sinusoidal drive. The displacement and maximum velocity of the speaker coil scales linearly with drive voltage, as predicted by the harmonic oscillator model.

The displacement and maximum velocity of the speaker coil scales roughly linearly with the drive voltage, as predicted by the harmonic oscillator model. Increasing the mass of the mirror qualitatively decreases the range and maximum velocity as expected. Since the total mass being driven by the speaker also includes the mass of the cone and the elastic membrane, reducing only the mass of the mirror does not linearly reduce the maximum displacement.

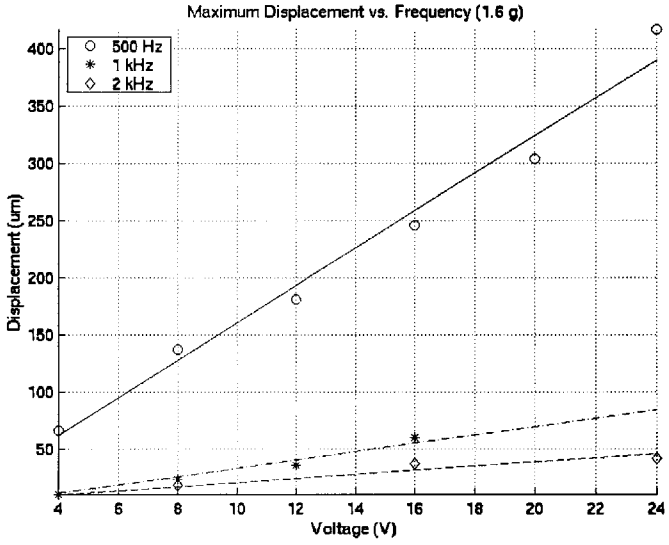

Figure 3.13 Displacement and maximum velocity versus for several sinusoidal drive frequencies. The maximum displacement decreases dramatically as frequency is increased.

Figure 3.13 shows a plot of the maximum displacement of the mirror as a function of the sinusoidal drive frequency. The displacement drops roughly by a factor of 4 when the drive frequency doubles from 500 Hz to 1 kHz. This is consistent with the SHO behavior described by equation 3.26, which predicts that for high frequencies and low damping, the displacement drops proportionally as the inverse square of the frequency. The displacement at 2 kHz, however, is inconsistent with this model. One likely explanation is that a resonant frequency of the system occurs near 2 kHz, which would explain the increase in displacement at that frequency as well as the increase in loudness of the speaker that was experimentally observed. The motion of the mirror also became difficult to measure at higher frequencies and at higher drive voltages because alignment error made the interferometric fringes difficult to detect. This is also consistent with driving near the resonance frequency and explains why fewer data points are shown for the 1 kHz and 2 kHz plots.

Linearity

Figure 3.14 shows typical linearity and velocity distribution plots for an 8 Volt sinusoidal drive at 500 Hz.

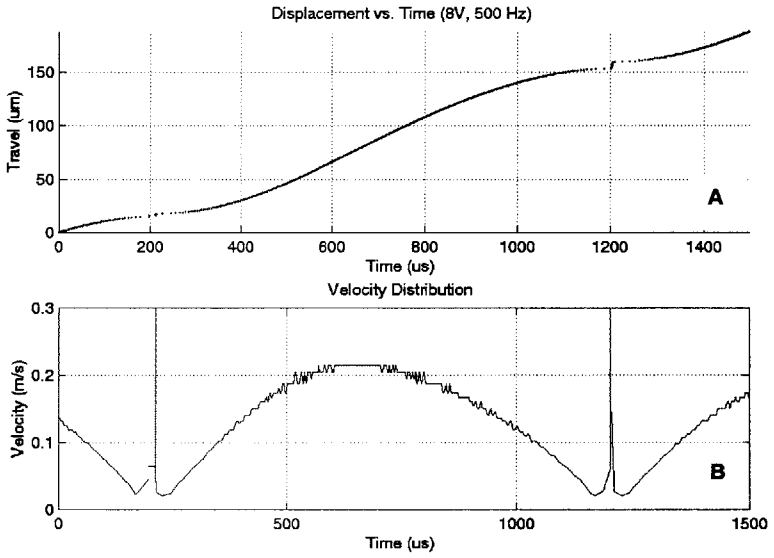

Figure 3.14 Typical linearity (A) and velocity distribution (B) for an 8 V sinusoidal drive waveform at 500 Hz. The displacement is plotted cumulatively over time.

The delay of the mirror is plotted cumulatively over time by determining the zero-crossing points in the interferogram and assigning a lambda/2 displacement to that time interval. The turning points of the drive correspond to points of zero velocity. The off-scale velocity values in this region correspond to overlapping zero crossing points contributed by noise error. The slight asymmetry that can be noticed in the velocity plot is due to nonlinearity in the drive waveform introduced by the stereo amplifier.

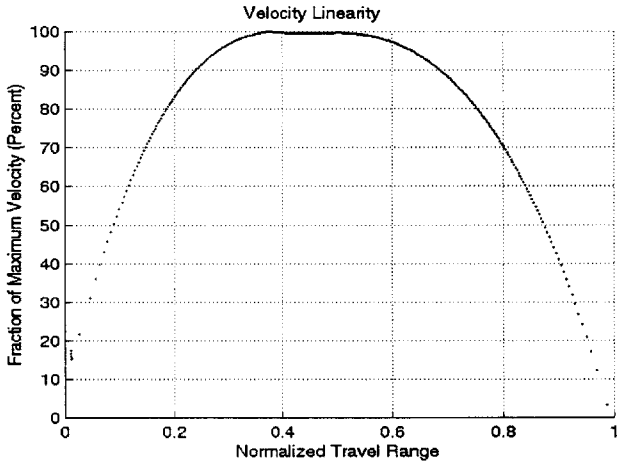

Figure 3.15 Velocity linearity as a function of normalized travel range.

Figure 3.15 is a plot of the velocity linearity as a function of the normalized travel range. The measured position of the mirror was subtracted from a linear scan to determine a percentage error which corresponds to a percentage change in velocity. For a 21-bounce cavity and a 10 Volt sinusoidal drive, the maximum peak-to-peak displacement for the speaker demonstrated in this chapter corresponds to 6.2 millimeters. A scan length of 2.7 millimeters can be achieved if a 10% deviation from the maximum velocity is acceptable. A bandpass filter with a center frequency of 9.5 MHz and a bandwidth of 950 kHz, corresponding to a Q factor of 10, would be used to optimize the dynamic range.

The waveform ultimately chosen to drive the speaker was a triangular drive that maximizes the useable linear scan range of the delay line. It was found that the square pulse waveforms used to approximate the delta drives caused significant mirror tilt during the scan, resulting in an alignment error which made the interferometric fringes difficult to detect. Xingde Li contributed

the software expertise to conduct this portion of the analysis. Orienting the speaker vertically reduced the alignment error due to weight imbalance, but a triangular drive is still preferred.

3.4 System Operation

After the linearity and the range of the optimum speaker have been determined, the flat mirror was removed and replaced with a concave gold mirror. The gold mirrors used in the delay line were both slotted to give clearance for the input and exit beams to enter and leave the cavity. The multi-pass cavity with one of the mirrors mounted on the speaker was then assembled on a portable breadboard and coupled into an existing *in vitro* OCT system.

3.4.1 Alignment and Actuation

A low coherence length light source with a 1.3 μm center wavelength was used for initial testing. A visible helium-neon aiming beam coupled into the *in vitro* system was used to align the delay line. Different cavity configurations were tested to determine the modulation on the power coupled back into the reference arm fiber. It was found that the positions of maximum beam stability, corresponding to minimum parasitic power modulation, corresponded well to the positions of minimum beam deviation presented previously.

In order to operate at one of the points of maximum beam stability, a double-pass configuration was required whereby the exit beam leaves the cavity and strikes a retroreflecting mirror before reentering the cavity and coupling into the reference arm. As one mirror of the delay line is scanned, the exit beam will in general exhibit both an angle deviation and a position deviation. A retroreflecting mirror has the property that any beam striking the surface is reflected back parallel to the original incident beam. The mirror therefore can therefore remove the effect of angle deviation by introducing a small parallel shift in the beam position. Any position deviation in the exit beam is also translated into a parallel position shift. The effect of a parallel position shift is a new input position *and* new angle for the beam coupling back into the fiber, resulting in parasitic modulation of the reference arm power. Setting the cavity at one of the zero

spot deviation separations minimizes the exit beam position deviation, and using a retroreflecting mirror minimizes parasitic modulation due to changes in the beam exit angle. The mirror was placed as close to the exit slot of the mirror as possible to minimize the position shift due to angle deviation. Discussions with Christian Chudoba aided in designing the final configuration of the delay line cavity.

Figure 3.16 shows the bounce pattern achieved on one mirror of the cavity. The speaker is oriented vertically to minimize alignment error due to weight imbalance during actuation. The input beam is coupled into the cavity through a cone-shaped aperture in the speaker magnet.

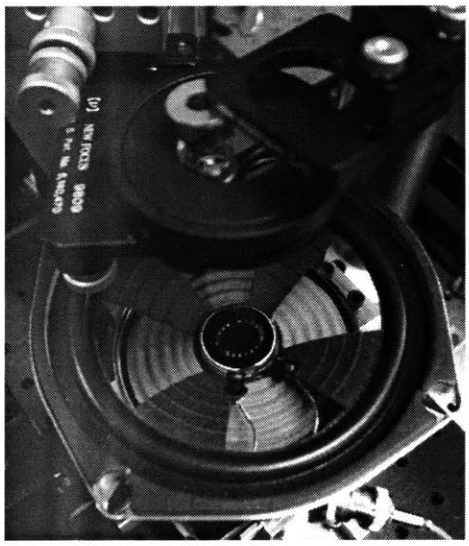

Figure 3.16 Photograph of the reflection pattern on one mirror produced by a He-Ne guiding beam. The cavity is operated with 21 bounces on each mirror, resulting in a total scan length of 42 times the mirror displacement. A retroreflector is used to redirect light back into the cavity to allow coupling back into the reference arm.

The delay line was aligned in a configuration that maximized the number of beam passes while optimizing the stability of the output beam. For ease of alignment, all components were mounted on optics mounts that allowed for tilt in two orthogonal directions. The exit mirror was also mounted such that the slot could be rotated and translated to align the optic axis and to select the appropriate exit beam.

3.4.2 Imaging

The delay line demonstrated in this section uses a pair of broadband gold mirrors in a Herriott cell configuration operated with 21 bounces on each mirror, yielding a path length scan of 42 times the mirror displacement. One end of the cavity is scanned using a commercial audio speaker. The system is operated in double-pass arrangement in which the exit beam is reflected back into the cavity to allow direct coupling back into the reference arm. A mirror separation of 9.2 cm was chosen to minimize beam deviation during actuation of one of the 20.32 cm radius mirrors in the cavity. The mirror is scanned with a displacement of 77 μm using a modified triangle waveform at 500 Hz, corresponding to a reciprocal scanning rate of 1 kHz.

An anesthetized *Xenopus laevis* (African frog) tadpole, a common developmental biology model, was used to demonstrate the feasibility of the Herriott delay line (Figure 3.17). The preliminary image was acquired using a 1.3 μm wavelength super-luminescent diode laser source with approximately 50 nm of optical bandwidth, corresponding to a 15 μm axial resolution in free space. Ravi Ghanta and Tony Ko assisted in operating the data acquisition system to obtain these images. The images were acquired using 3 mW of incident optical power. The image consists of 3000 axial scans with 1000 pixels per axial scan. The scan velocity produced by the delay line is 3.3 m/s, corresponding to a Doppler frequency of approximately 5 MHz.

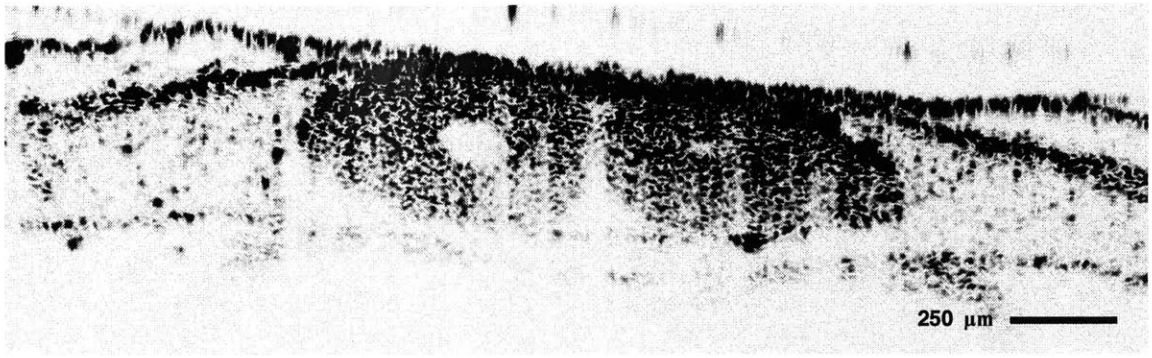

Figure 3.17 Preliminary image of the dorsal side of a *Xenopus laevis* tadpole acquired using a Herriott cell delay line. The image was acquired at a 1 kHz repetition frequency.

The pictured scale bar represents 250 μm. The total axial range of the scan was 3.1 mm, corresponding to 2.1 mm in tissue. A thin glass slide was placed above the specimen to reduce backscattering due to index mismatch at the air-tissue interface. A bandpass filter centered at 5 MHz with a 250 kHz bandwidth was used in the acquisition of the above image, yielding a signal-to-noise figure of 95 dB. Ingmar Hartl assisted and provided advice in designing the filters for the data acquisition electronics. A filter bandwidth of at least 180 kHz is required to support 15 μm resolution at 5 MHz. In order to support both the spectral bandwidth and a 10% deviation from the linear region, a filter bandwidth of 680 kHz would be required. The smaller bandwidth filter was used to improve the dynamic range for these images while trading off scan length. The image was also post-processed to reduce jitter artifact produced by the speaker. The final image was cropped to remove the glass slide and inertial motion artifacts produced by the transverse scanning stage. Active filters with higher a higher Q value and sharper roll-off near the band edges are currently being investigated to improve the dynamic range without sacrificing scan length.

3.5 Discussion

Several avenues are currently being investigated to optimize the Herriott delay line to determine if permanent integration into an existing OCT system is feasible. One issue with the multi-pass scanning concept is that the system is inherently sensitive to small displacements. It was found that the zero-position of the scan was only stable to within roughly 2 μm at 500 Hz and 7 μm at 1 kHz. This corresponds to about 1 % and 20 % of the total scan range for 500 Hz and 1 kHz, respectively. This jitter exhibited a periodic cycle with a frequency corresponding roughly to 60 Hz. The jitter was therefore determined to be a result of amplified AC line noise. A better quality stereo amplifier is currently being used which enables scanning at a 2 kHz repetition frequency over 3.1 mm with 1.5% jitter. The detection electronics is currently being designed to accommodate the high heterodyne modulation frequencies and broad bandwidths required to support high resolution imaging.

A higher scan range may also be achieved by increasing the number of passes in the cavity using astigmatic mirrors. Herriott has shown that distorting the mirrors to add a cylindrical component can result in complex Lissajous bounce patterns that efficiently cover the mirror surface[35]. The amount of distortion required is small, often as little as a few fringes of the operating wavelength. This would reduce the drive voltage required to achieve a useable scan range, potentially increasing the operating frequency for a given acceptable level of reference arm power modulation.

An alternative Herriott delay line configuration can also be envisioned whereby a mirror is mounted on a high field ceramic magnet. Electromagnetic actuation can be achieved by mounting the magnet within a wire coil and passing an alternating current through the coil to generate an alternating magnetic field. The advantage of driving a magnet with a fixed coil rather than a coil with a fixed magnet is that the coil can be externally cooled, allowing higher drive powers to be used. Rare earth magnets with exceptionally strong field strengths are now commercially available, allowing the combined mirror and magnet mass to be made quite small. The cavity can be rebuilt with smaller radii of curvature mirrors, reducing the cavity separation and reducing the free space path length in the reference arm. This would ease the task of dispersion-matching the sample and reference arms of the system, which is necessary for ultrahigh resolution OCT imaging with new broad bandwidth laser sources. Using an alternate method of actuating the mirror would also permit greater input beam angles, allowing alternate spot patterns to be chosen.

Chapter 4

Summary and Conclusion

A high-speed scanning optical delay line has been developed based on a Herriott cell multi-pass cavity and electromagnetic actuation. The delay line is demonstrated to achieve path length scanning at a 1 kHz repetition frequency over 3.1 mm. The system enables image acquisition at a rate of 4 frames per second, allowing motion-artifact free *in vivo* OCT images to be obtained. Higher scan ranges and repetition frequencies are presently feasible. The dynamic range of the system is currently 95 dB over 25% of the total scan. Filtering techniques are being investigated to further improve the dynamic range without sacrificing scan range.

Using an audio speaker and a multi-pass configuration, a high-speed optical delay line based on a Herriott cavity has been demonstrated for the first time. The highest speed scanning technique currently available, the grating-based phase delay line, has spectral bandwidth limitations which are not well-characterized. The limitations of currently available scanning methods, in combination with the recent development of new broad bandwidth laser sources, have motivated the investigation of alternative high-speed scanning techniques. A portable, low-cost, high-speed optical delay line capable of supporting broad bandwidths would allow OCT to be used in the clinical setting to provide spectroscopically-resolved *in vivo* images of tissue microstructure with resolutions approaching that of histopathology. The availability of such an imaging modality would significantly impact the standard of health care and allow physicians to guide biopsy to reduce patient morbidity and mortality associated with sampling error,

potentially detect neoplastic changes associated with many types of early stage pathologies, and increase the effectiveness of medical intervention.

The model and experimental results for the Herriot cell delay line indicate that this technique is a feasible alternative to current high-speed scanning methods. The delay line outperforms standard linear mechanical scanning, is inexpensive, and is easy to optimize and align based on the results presented in this thesis. The technique can also be scaled upwards to match and potentially exceed the scan frequency of the grating-based phase delay line, the current high-speed standard, without complications due to inherent bandwidth limitations. The Herriott cell delay line has the advantages of high-speed, low cost, and the ability to support broad bandwidths, and can feasibly replace all currently used methods for high-speed scanning.

References

[1] D. Huang, E. Swanson, C. Lin, J. Schuman, W. Stinson, W. Chang, M. Hee, T. Flotte, K. Gregory, C. Puliafito and J. Fujimoto, "Optical coherence tomography," Science, vol. **254**, pp. 1178-1181, (1991).

[2] J. Fujimoto, M. Brezinski, G. Tearney, S. Boppart , B. Bouma, M. Hee, J. Southern and E. Swanson, "Optical biopsy and imaging using optical coherence tomography," Nature Medicine, vol. **1**, pp. 970-2, (1995).

[3] M. Brezinski, G. Tearney, B. Bouma, J. Izatt, M. Hee, E. Swanson, J. Southern and J. Fujimoto, "Optical coherence tomography for optical biopsy: properties and demonstration of vascular pathology," Circulation, vol. **93**, pp. 1206-13, (1996).

[4] G. Tearney, M. Brezinski, B. Bouma, S. Boppart, C. Pitris, J. Southern and J. Fujimoto, "In vivo endoscopic optical biopsy with optical coherence tomography," Science, vol. **276**, pp. 2037-9, (1997).

[5] K. Takada, I. Yokohama, K. Chida and J. Noda, "New measurement system for fault location in optical waveguide devices based on an interferometric technique," Applied optics, vol. **26**, pp. 1603-8, (1987).

[6] H. Gilgen, R. Novak, R. Salathe, W. Hodel and P. Beaud, "Submillimeter optical reflectometry," IEEE J Lightwave Technology, vol. **7**, pp. 1225-33, (1989).

[7] R. Youngquist, S. Carr and D. Davies, "Optical coherence-domain reflectometry: a new optical evaluation technique," Optics Letters, vol. **12**, pp. 158-60, (1987).

[8] F. Kremkau, Diagnostic ultrasound: principles, instrumentation, and exercises, 2nd ed. Philadelpha: Grune and Stratton, 1984.

[9] F. Kremkau, Doppler ultrasound: Principles and instruments. Philadelphia: W. B. Saunders, 1990.

[10] P. Fish, Physics and instrumentation of diagnostic medical ultrasound. New York: John Wiley and Sons, 1990.

[11] W. Ziebel and R. Sohaey, Introduction to ultrasound. Philadelphia: W. B. Saunders, 1998.

[12] E. Swanson, D. Huang, M. Hee, J. Fujimoto, C. Lin and C. Puliafito, "High speed optical coherence domain reflectometry," Optics Letters, vol. **17**, pp. 151-3, (1992).

[13] E. Swanson, J. Izatt, M. Hee, D. Huang, C. Lin, J. Schuman, C. Puliafito and J. Fujimoto, "In vivo retinal imaging by optical coherence tomography," Optics Letters, vol. **18**, pp. 1864-66, (1993).

[14] A. Sergeev, V. Gelikonov, G. Gelikonov, F. Feldchtein, R. Kuranov, N. Gladkova, N. Shakhova, L. Suopova, A. Shakhov, I. Kuznetzova, A. Denisenko, V. Pochinko, Y. Chumakov and O. Streltzova, "In vivo endoscopic OCT imaging of precancer and cancer states of human mucosa," Optics Express, vol. **1**, pp. 432-40, (1997).

[15] G. Tearney, B. Bouma and J. Fujimoto, "High speed phase- and group delay scanning with a grating-based phase control delay line," Optics Letters, vol. **22**, pp. 1811-13, (1997).

[16] A. Rollins, M. Kulkarni, S. Yazdanfar, R. Ung-arunyawee and J. Izatt, "In vivo video rate optical coherence tomography," Optics Express, vol. **3**, (1998).

[17] B. Bouma, G. Tearney, I. Bilinsky, B. Golubovic and J. Fujimoto, "Self-phase-modulated Kerr-lens mode-locked Cr:forsterite laser source for optical coherence tomography," Optics Letters, vol. **21**, pp. 1839-42, (1996).

[18] W. Drexler, U. Morgner, F. Kartner, C. Pitris, S. Boppart, X. Li, E. Ippen and J. Fujimoto, "In vivo ultrahigh resolution optical coherence tomography," Optics Letters, vol. **24**, pp. 1221-23, (1999).

[19] U. Morgner, W. Drexler, F. Kaertner, X. Li, C. Pitris, E. Ippen and J. Fujimoto, "Spectroscopic optical coherence tomography," Optics Letters, vol. **25**, pp. 111-3, (2000).

[20] J. Ballif, R. Gianotti, P. Chavanne, R. Walti and R. Salathe, "Rapid and scalable scans at 21 m/s in optical low-coherence reflectometry," Optics Letters, vol. **22**, pp. 757-9, (1997).

[21] C. Su, "Achieving variation of the optical path length by a few millimeters at millisecond rates for imaging of turbid media and optical interferometry: a new technique," Optics Letters, vol. **22**, pp. 665-7, (1997).

[22] Z. Yasa and N. Amer, "A rapid-scanning autocorrelation scheme for continuous monitoring of picosecond laser pulses," Optics Communications, vol. **36**, pp. 406-8, (1981).

[23] L. Beiser and R. Johnson, Scanners, Handbook of Optics, vol. 2, 2nd ed. New York: McGraw Hill, Inc., 1995.

[24] G. Tearney, B. Bouma, S. Boppart, B. Golubovic, E. Swanson and J. Fujimoto, "Rapid acquisition of *in vivo* biological images by use of optical coherence tomography," Optics Letters, vol. **21**, pp. 1408-10, (1996).

[25] V. Gelikonov, G. Gelikonov, N. Gladkova, V. Leonov, F. Feldchtein, A. Sergeev and Y. Khanin, (1998).

[26] V. Gelikonov, G. Gelikonov, N. Gladkova, V. Leonov, F. Feldchtein, A. Sergeev and Y. Khanin, (1999).

[27] I. PiezoMech, Catalog. 15 W 700 North Frontage Road Suite 134, Hinsdale, Illinois, 60521-7568: PiezoMech, Inc.

[28] J. Heritage, A. Weiner and R. Thurston, "Picosecond pulse shaping by spectral phase and amplitude manipulation," Optics Letters, vol. **10**, pp. 609-11, (1985).

[29] R. Thurston, J. Heritage, A. Weiner and W. Tomlinson, "Analysis of picosecond pulse shape synthesis by spectral masking in a grating pulse compressor," IEEE J Quantum Electronics, vol. **QE-22**, pp. 682-96, (1986).

[30] G. Tearney. (1996). "In Vivo Optical Coherence Tomography," , Massachusetts Institute of Technology, Cambridge.

[31] D. Herriott, H. Kogelnik and R. Kompfner, "Off-axis paths in spherical interferometers," Applied Optics, vol. **3**, pp. 523-6, (1964).

[32] D. Herriott and H. Schulte, "Folded optical delay lines," Applied Optics, vol. **4**, pp. 883-9, (1965).

[33] J. McManus and P. Kebabian, "Narrow optical interference fringes for certain set-up conditions in multi-pass absorption cells of Herriott type," Applied Optics, vol. **29**, (1990).

[34] J. Silver and A. Stanton, "Optical interference fringe reduction in laser absorption experiments," Applied Optics, vol. **27**, pp. 1914-6, (1988).

[35] W. Trutna and R. Byer, "Multiple-pass Raman gain cell," Applied Optics, vol. **19**, pp. 301-12, (1980).

[36] J. Altmann, R. Baumgart and C. Weitkamp, "Two-mirror multipass absorption cell," Applied Optics, vol. **20**, pp. 995-9, (1981).

[37] D. Kaur, A. de Souza, J. Wanna, A. Hammad Sammeer, L. Mercorelli and D. Perry, "Multiples cell for molecular beam absorption spectroscopy," Applied Optics, vol. **29**, pp. 119-24, (1990).

[38] J. McManus, P. Kebabian and M. Zahniser, "Astigmatic mirror multipass absorption cells for long-path-length spectroscopy," Applied Optics, vol. **34**, pp. 3336-48, (1995).

[39] A. Siegman, Lasers. Mill Valley, CA: University Science Books, 1986.

List of Figures

Chapter 1

Chapter 2

Chapter 3

Figure 3.9 Plot of spot deviation versus normalized cavity separation for the first 4 round trips on mirror 1 The number of zero deviation configurations increases with the number of round trip passes.

Figures 3.10 Plot of spot deviation versus normalized cavity separation for the 22nd round trip.

Figure 3.11 Cutaway view of a speaker coil and magnet. Passing an alternating current through the coil causes the coil to actuate at the frequency of the driving voltage.

Figure 3.12 Displacement and maximum velocity versus voltage plots for an 8 Volt sinusoidal drive. The displacement and maximum velocity of the speaker coil scales linearly with drive voltage, as predicted by the harmonic oscillator model.

Figure 3.14 Typical linearity and velocity distribution for an 8 V sinusoidal drive waveform at 500 Hz. The displacement is plotted cumulatively over time.

Figure 3.15 Velocity linearity for an 8 Volt sinusoidal drive as a function of normalized travel range.

Figure 3.16 Photograph of the reflection pattern on one mirror produced by a He-Ne guiding beam. The cavity is operated with 21 bounces on each mirror, resulting in a total scan length of 42 times the mirror displacement.

Figure 3.17 Preliminary image of the dorsal side of a *Xenopus laevis* tadpole acquired using a Herriott cell delay line. The image was acquired at a 1 kHz repetition frequency.